Surface Radiation Exchange for Two-Dimensional Rectangular Enclosures Using the Discrete-Ordinates Method

A. Sànchez
Research Assistant.

T. F. Smith
Professor.
Mem. ASME

Department of Mechanical Engineering,
The University of Iowa,
Iowa City, IA 52242

The purpose of this study is to develop a model based on the discrete-ordinates method for computing radiant exchange between surfaces separated by a transparent medium and to formulate the model so that arbitrary arrangements of the surfaces can be accommodated. Heat fluxes from the model are compared to those based on the radiosity/irradiation analysis. Three test geometries that include shadowing and irregular geometries are used to validate the model. Heat fluxes from the model are in good agreement with those from the radiosity/irradiation analysis. Effects of geometries, surface emittances, grid patterns, finite-difference weighting factor, and number of discrete angles are reported.

Introduction

Radiant exchange between surfaces separated by a radiatively nonparticipating medium occurs in numerous engineering applications including building interior thermal environments, electronic thermal control, solar energy usage, and spacecraft thermal control. In most applications, the components and enclosures are not simple geometries, and effects of shadowing, obstructing views, and irregularities must be taken into account. There exists, therefore, a need to develop methods that enable these and other factors to be included in a radiant exchange analysis. Several techniques are available for performing a radiant exchange analysis for surfaces separated by a transparent medium. Among them are the radiosity/irradiation method (RIM) (Sparrow and Cess, 1978; Siegel and Howell, 1981), the ray tracing technique (Greenberg, 1989; Baumeister, 1990), the Monte Carlo method (Siegel and Howell, 1981), and the stochastic method based on Markov chains (Naraghi and Chung, 1984, 1986; Billings et al., 1990). The ray tracing and Monte Carlo techniques have the capabilities of handling complex geometries but suffer from excessive computational times and uncertainties as to the number of rays needed to produce accurate results. View factors are fundamental to the RIM. Conceptually, view factors can be evaluated for complex geometries but difficulties arise when shadowing and obstructing effects are present. Recent computational advances have reduced the effort required to compute the view factors for complex enclosures (Walton, 1987; Greenberg, 1989; Rushmeier et al., 1990; Emery et al., 1991). Despite these techniques, there still exists a need for methods than can be applied conveniently to complex enclosures and that can be interfaced with models for other modes of heat transfer.

The discrete-ordinates method (DOM) (Fiveland, 1988; Sànchez et al., 1991) has undergone considerable development for analyzing radiant transfer in participating media, but has yet to be applied to radiant exchange for surfaces separated by a nonparticipating medium. For gaseous participating media, the spectral variation of the radiative properties is modeled as a series of absorbing bands separated by windows that are radiatively nonparticipating. Modest (1991) indicates that nongray effects for participating media can be accounted for in the general radiative transfer equation by using the weighted-sum-of-gray-gases model (WSGGM). Inherent within the WSGGM is the stipulation that an absorption coefficient is assigned a zero value to represent the transparent windows between absorbing bands. Hence, the accuracy of using the DOM to model radiant exchange within nonparticipating media needs to be established.

The objective of this study is to examine the feasibility of applying the DOM to the problem of computing the radiant exchange between surfaces separated by a transparent medium. The basic idea is to apply the general DOM to enclosures and to set some radiative properties in the DOM to some values in order to represent an opaque solid within the enclosure. Radiant exchange between surfaces forming the opaque solid and the other surfaces of the enclosure is then embedded within the DOM. The idea is based on the method used to solve flow and heat transfer problems in a domain containing both solid and fluid control volumes (conjugate heat transfer) (Patankar, 1990; House et al., 1990). In that method, the viscosity of a solid control volume is assigned a large value to force velocities to zero and the thermal conductivity of a solid control volume is assigned that of the solid.

Analysis

System Description. A generalized two-dimensional rectangular enclosure selected for study is shown in Fig. 1. The enclosure has a height H and width L. The walls are considered the boundary of the solution domain within which the radiant exchange is taking place. The enclosure may contain several protrusions mounted on the walls and obstructions, all of which contribute to the effects of multiple surfaces and shadowing. The protrusions and obstructions are opaque to radiation. Surfaces forming the enclosure, protrusions, and obstructions are diffusely emitting and reflecting, opaque, and gray and may have nonuniform radiative property and temperature distributions. The radiative properties are independent of temperature. Openings represented by pseudoblack surfaces could form a part of the enclosure walls. The intervening medium is radiatively transparent. As described later, three geometries of the generalized enclosure are configured to verify the accuracy of the DOM.

Radiative Transfer Equations. The governing radiative transfer equations for radiant exchange in a participating me-

Contributed by the Heat Transfer Division for publication in the JOURNAL OF HEAT TRANSFER. Manuscript received by the Heat Transfer Division April 10, 1991; revision received September 11, 1991. Keywords: Numerical Methods, Radiation, Radiation Interactions.

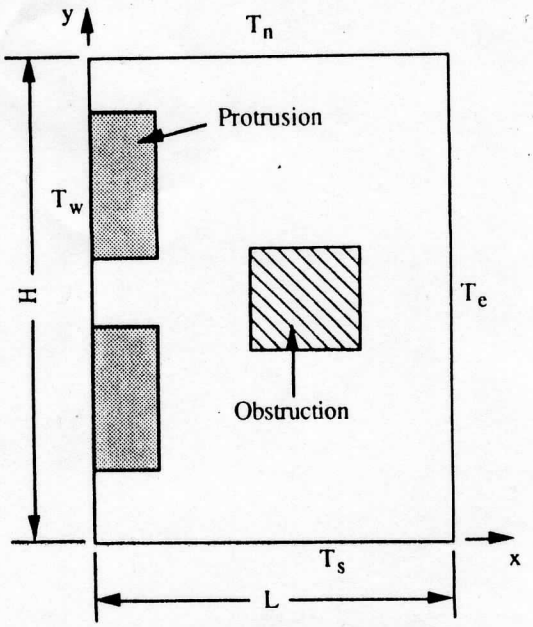

Fig. 1 Schematic diagram of typical enclosure

dium and the boundary conditions are presented to illustrate the nature of the problem that is being approximated. The radiative transport equation for the intensity for an absorbing and emitting medium is

$$\frac{\partial I}{\partial \xi} = -\kappa I + \kappa I_b \tag{1}$$

where ξ is the line-of-sight distance in the direction of propagation of the radiant intensity I, κ is the absorption coefficient of the medium, and I_b is the local blackbody intensity. Opaque and transparent media are represented by large and small values of the absorption coefficient, respectively. For a large value of the absorption coefficient, the intensity equals the blackbody intensity, and for an absorption coefficient of zero, the intensity remains unchanged. For a two-dimensional system, Eq. (1) is expressed as

$$\mu \frac{\partial I}{\partial x} + \eta \frac{\partial I}{\partial y} = -\kappa I + \kappa I_b \tag{2}$$

where $I = I(x, y; \mu, \eta)$, $I_b = I_b(x, y)$, and μ and η are direction cosines. At an opaque surface, the leaving intensity is composed of the emitted intensity and the reflected irradiation and is written as

$$I(x_a, y_a; \mu, \eta) = \epsilon I_b(x_a, y_a) + \frac{\rho}{\pi} \int_{2\pi} I'(x_a, y_a; \mu', \eta') \cos \phi' \, d\omega' \tag{3}$$

where the subscript a denotes a surface, ϵ is the surface emittance, and ρ is the surface reflectance ($= 1 - \epsilon$). The prime denotes an incoming quantity, ϕ is the polar angle between the surface normal and the intensity, and ω is the solid angle. The integration in Eq. (3) is performed over the hemisphere above the surface. The net radiant energy leaving a surface is the difference between the radiosity and irradiation and is given by

$$q(x_a, y_a) = \int_{2\pi} I(x_a, y_a; \mu, \eta) \cos \phi \, d\omega - \int_{2\pi} I'(x_a, y_a; \mu', \eta') \cos \phi' \, d\omega' \tag{4}$$

Equations (1)-(4) apply on either a spectral or a gray basis. Equations (1)-(4) are the radiative transfer expressions being approximated.

Discrete-Ordinates Method. The development of the discretized form of the radiative transfer equations is initiated by subdividing the solution domain into a number of control volumes. Control volume P surrounded by control volumes E, S, W, and N is illustrated in Fig. 2(a). The interfaces between control volume P and the surrounding control volumes are designated by e, s, w, and n. In addition to the spatial discretization, the directions of propagation of the radiant intensity are discretized.

The intensity at point P in discrete direction i is I_i^P. For the positive x direction and for the ith direction, intensities entering and leaving control volume P are I_i^{wr}, I_i^{sr} and I_i^e, I_i^n. For the negative x direction, the corresponding intensities can be defined. The radiative properties of the w interface are denoted by ϵ_w, τ_w, and ρ_w for emittance, transmittance, and reflectance. Similarly, the radiant intensities and radiative properties of the other three interfaces can be introduced.

Application of Eq. (2) to discrete direction i yields

$$\mu_i \frac{\partial I_i}{\partial x} + \eta_i \frac{\partial I_i}{\partial y} = -\kappa_P I_i + \kappa_P I_b \tag{5}$$

where $I_i = I(x, y; \mu_i, \eta_i)$ and $i = 1$ to 4 M with M denoting the number of discrete angles within a quadrant. The finite-dif-

Nomenclature

A = area, m^2
e_{max} = maximum error, percent
e_{rms} = root-mean-square error, percent
F_{i-j} = view factor between surfaces i and j
H = dimension of enclosure, m
I = radiant intensity, W/m^2-sr
K = surface location number
L = dimension of enclosure, m
N = number of surfaces exchanging radiant energy
M = number of discrete angles per quadrant
nx, ny = number of control volumes for x and y directions
q = net radiant energy leaving, W/m^2
T = temperature, K
V = volume, m^3
w = quadrature weighting factor
x = coordinate, m
y = coordinate, m
α = finite-difference weighting factor
ϵ = emittance
ζ = dimensionless distance
η = direction cosine
κ = absorption coefficient, m^{-1}
μ = direction cosine
ξ = distance along line-of-sight direction, m
ρ = reflectance
σ = Stefan-Boltzmann constant, 5.669×10^{-8} W/m^2-K^4
τ = transmittance
ϕ = polar angle
ω = solid angle, sr

Subscripts

a = surface area element
b = blackbody
e = east
n = north
s = south
w = west

Superscripts

e = east
n = north
r = entering
s = south
w = west
$'$ = incident quantity

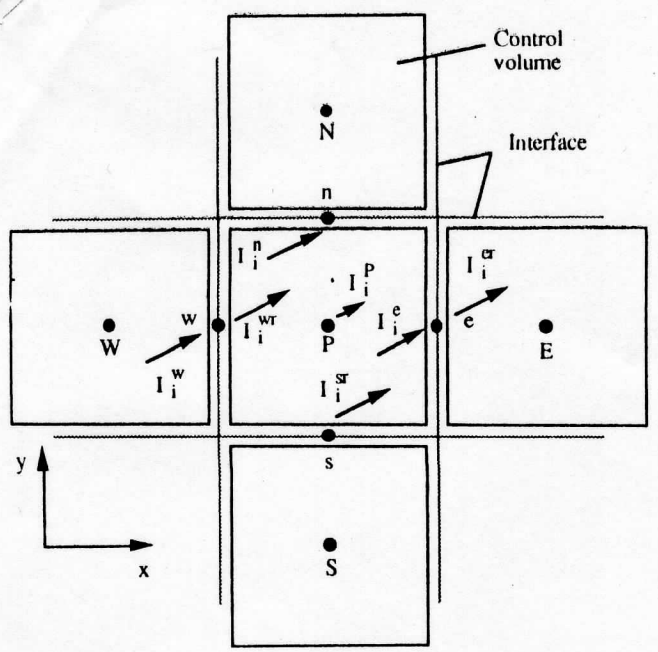

(a) Control volumes.

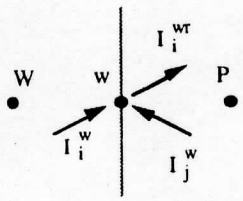

(b) Interface.

Fig. 2 Control volumes and interfaces

ference form of Eq. (5) is derived by applying this expression to the control volume P, multiplying by $\Delta x \Delta y$, and integrating over the four faces of the control volume to yield

$$\mu_i A_x (I_i^e - I_i^{wr}) + \eta_i A_y (I_i^n - I_i^{sr}) + \Delta V_P \kappa_P I_i^P = \Delta V_P \kappa_P I_b^P \quad (6)$$

where $A_x = \Delta y$, $A_y = \Delta x$, and $\Delta V_P = \Delta x \Delta y$. The leaving intensities at the e and n interfaces are approximated by

$$I_i^e = \frac{1}{\alpha} [I_i^P - (1-\alpha) I_i^{wr}] \quad (7a)$$

$$I_i^n = \frac{1}{\alpha} [I_i^P - (1-\alpha) I_i^{sr}] \quad (7b)$$

α is the finite-difference weighting factor. Inserting Eqs. (7a) and (7b) into Eq. (6) and solving for I_i^P yield

$$I_i^P = \frac{|\mu_i| A_x I_i^{wr} + |\eta_i| A_y I_i^{sr} + \alpha \kappa_P I_b^P \Delta V_P}{|\mu_i| A_x + |\eta_i| A_y + \alpha \kappa_P \Delta V_P} \quad (8)$$

Application of Eq. (8) to the problem of radiative transfer for solid and transparent control volumes begins by first noting that, for a transparent control volume, $\kappa_P = 0\ \mathrm{m}^{-1}$ and, for a solid control volume, κ_P is assigned a very large value to simulate a highly attenuating medium (for example, $\kappa_P = 10^{20}\ \mathrm{m}^{-1}$). For these two situations, Eq. (8) reduces to:

Transparent Medium

$$I_i^P = \frac{|\mu_i| A_x I_i^{wr} + |\eta_i| A_y I_i^{sr}}{|\mu_i| A_x + |\eta_i| A_y} \quad (9a)$$

and

Table 1 Property relations

(a) Interior control volumes

Control volume*		Radiative properties for w-interface			Radiant intensity for w-interface
W	P	ϵ_w	τ_w	ρ_w	I_i^{wr}
T	T	0	1	0	I_i^w
S	S	0	0	1	$\frac{1}{\pi}\sum_{j=1}^{2M} w_j \mu_j I_j^w$
S	T	ϵ_w	0	$1-\epsilon_w$	$\epsilon_w I_{bw} + \frac{\rho_w}{\pi}\sum_{j=1}^{2M} w_j \mu_j I_j^w$
T	S	ϵ_w	0	$1-\epsilon_w$	$\epsilon_w I_{bw} + \frac{\rho_w}{\pi}\sum_{j=1}^{2M} w_j \mu_j I_j^w$

* S - solid; T - transparent

(b) Boundary control volume

- Control volume P is transparent: ϵ_w = given, $\rho_w = 1 - \epsilon_w$
- Control volume P is solid: $\epsilon_w = 0$, $\rho_w = 1$

Solid Medium

$$I_i^P = I_b^P \quad (9b)$$

To verify Eq. (9a), consider radiation that propagates only in the x direction. Hence, $\eta_i = 0$ and Eq. (9a) reduces to

$$I_i^P = I_i^{wr} \quad (10)$$

This relation implies that, as expected, the intensity does not change in the direction of propagation as the radiation passes through a transparent medium.

The entering intensities must now be related to those leaving the control volumes. Consider interface w. The radiant intensities of interface w are shown in Fig. 2(b), where the leaving intensity for control volume P in the discrete direction j is I_j^w. For an interface, I_j^w may be transmitted through the interface or reflected by the interface into the ith direction. In terms of the radiative properties of the interfaces, the intensity entering control volume P from the w interface is evaluated by

$$I_i^{wr} = \tau_w I_i^w + \epsilon_w I_{bw} + \frac{\rho_w}{\pi} \sum_{j=1}^{2M} w_j \mu_j I_j^w \quad (11)$$

where I_{bw} is the blackbody intensity evaluated at the temperature of the w interface, and w_j are the angular quadrature weights for the j direction. The summation in Eq. (11) is over only those quadrants within a transparent control volume and only performed when the W control volume is opaque. A similar expression for the entering intensity I_i^{sr} for the s interface can be written.

The radiative properties of the interface between two control volumes are identified next. Specifically, for the w interface, the radiative properties of the interface are assigned the values stated in Table 1(a). The interface properties depend on the characteristics of the adjacent control volumes. For all cases, $\rho_w = 1 - \epsilon_w - \tau_w$. Hence, only two radiative properties of an interface, namely, ϵ_w and τ_w, need to be specified. Intensities I_i^{wr} derived from Eq. (11) for the various combinations are also stated.

Figure 3 applies for a control volume adjacent to a boundary of the enclosure; the interface w is considered to be a boundary node. The intensity leaving this face is

$$I_i^{wr} = \epsilon_w I_{bw} + \rho_w \sum_{j=1}^{2M} w_i \mu_j I_j^w \qquad (12)$$

The conditions of the radiative properties are itemized in Table 1(*b*) for the two possible characteristics of control volume *P*, namely, opaque and transparent.

The net radiant energy leaving an interface is evaluated from the difference between the radiosity and irradiation. The expression for the radiant heat flux for interface *w* is

$$q_w = \sum_{i=1}^{2M} w_i \mu_i I_i^{wr} - \sum_{i=1}^{2M} w_i \mu_i I_i^w \qquad (13)$$

The summations in Eq. (13) are for the four quadrants forming the entire space around interface *w* and include only those quadrants where the medium is transparent. If all quadrants cover a solid or cover a transparent medium, the radiant flux is zero. For a boundary control volume, the summations are over the hemisphere on the inside of the enclosure.

An important aspect of the DOM is the selection of the weighting factors and direction cosines for approximation of the hemispherical integrations. For surface radiant exchange, only the half-range heat fluxes need to be considered. They can be approximated by

$$\pi = 2\int_0^1 \mu d\mu = 2\sum_{i=1}^{M} w_i \mu_i \qquad (14)$$

After experimenting with several quadrature sets (Truelove, 1987; Fiveland, 1988), a set based on equal weights and an equal angular increment of the polar angle ϕ was generated. The discretized polar angles for $i=1$ to M are $\phi_i = \Delta\phi/2 + (i-1)\Delta\phi$, where $\Delta\phi = \pi/2M$, and the equal weights are

$$w = \pi/2 \sum_{i=1}^{M} \cos \phi_i \qquad (15)$$

Heat fluxes computed using these weights and direction cosines are found to be more accurate than those using the other quadrature sets. The current set, however, may not be the optimum set.

Another important consideration is the selection of the value for the finite-difference weighting factor. Initially, this factor was taken as a constant, for example, $\alpha = 0.5$ or 1.0. However, values of radiant intensities for some of the transparent control volumes (opaque control volumes are not of concern) were found outside the range of physically allowable values. Therefore, for each discrete direction and spatial location, a check is made that the control volume intensity computed from Eq. (8) is bounded by the incoming intensities, for example, the south and west intensities in Fig. 2(*a*). If the check fails, the control volume intensity is assigned either the minimum or maximum of the incoming intensities. The leaving intensities given by Eqs. (7*a*) and (7*b*) are computed and compared to the minimum and maximum intensities. If the comparison fails, the value of α is increased by $\Delta\alpha$, taken as 0.01, and new leaving intensities are computed. In most cases, only one increment of the initial value of α is required. This procedure is continued until a leaving intensity is within the bounds; the other leaving intensity is then computed from Eq. (6). The values of α reported later are the initial values.

The solution procedure for the radiant intensities is similar to that used by Sànchez et al. (1991). An iterative procedure with sweeps for each of the two spatial directions and the four quadrants is necessary to solve for the intensities. Convergence of the intensities occurs when the variation in the intensity between iterations is less than an error criterion, taken as 1.0×10^{-3} percent.

The accuracy of the DOM is verified in part by checking that the overall energy balance is zero. The overall energy balance is computed by summing the product of the radiant heat flux and surface area for each interface and for all boundary surfaces.

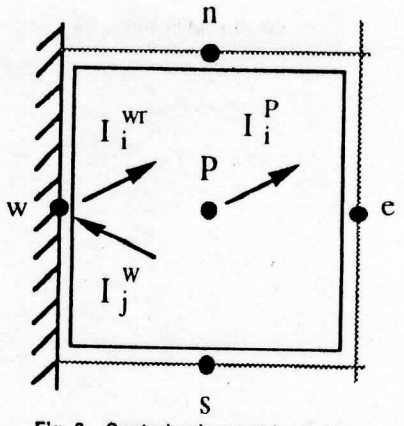

Fig. 3 Control volume at boundary

The DOM may be used to compute the view factors between any two opaque surfaces when all surfaces are black. If the view factor between surface *i* and surface *j* is sought, the blackbody emissive power of surface *i* is set equal to unity and that for all other surfaces is set equal to zero. The absolute value of the radiant flux for surface *j* is equal to the view factor F_{j-i}. Reciprocity gives the view factor F_{i-j}. Alternatively, the view factors could be evaluated from the set of equations given by

$$q_i = \sigma \sum_{j=1}^{N} F_{i-j}(T_i^4 - T_j^4) \qquad (16)$$

which are solved simultaneously for F_{i-j}. In Eq. (16), N is the number of opaque surfaces within the enclosure and is determined by considering the interfaces between control volumes in Figs. 2 and 3. In view of the desire to compute radiant heat fluxes for general geometries as shown in Fig. 1, this study concentrates on the radiant heat fluxes.

Radiosity/Irradiation Method. Heat fluxes for the DOM are compared to those obtained from a radiant exchange analysis based on the RIM. For the RIM, the enclosure, including all protrusions and obstructions, is divided into N isothermal surfaces each with uniform irradiation, radiosity, and view factor. View factors are determined exactly using the cross-string method (Siegel and Howell, 1981), and all shadowing and occulting effects, when present, are taken into account. View factors computed using the cross-string method are interpreted as integrated values over a surface element. The reciprocity relation is used to reduce the number of view factors that must be found. For each surface, the enclosure relation is verified. Calculations from the RIM are checked to verify that the overall energy balance for the enclosure is zero.

Results and Discussion

The accuracy of the DOM is examined by configuring three test cases, namely, (1) a rectangular enclosure with no protrusions and obstructions, (2) a rectangular enclosure with a centered obstruction, and (3) a rectangular enclosure with two protrusions. Case 1 is used to examine in greater detail some of the characteristics of the DOM. Cases 2 and 3 exhibit shadowing and irregular geometry effects.

In addition to the radiative properties of the surfaces and the temperatures, solutions for the DOM depend on the selection of the finite-difference weighting factor, the number of discrete angles, and the grid spacing. Hence, one goal of the comparisons is to establish values of these parameters that yield accurate radiant heat fluxes. Heat fluxes for the DOM for all cases are computed using a single program, where only

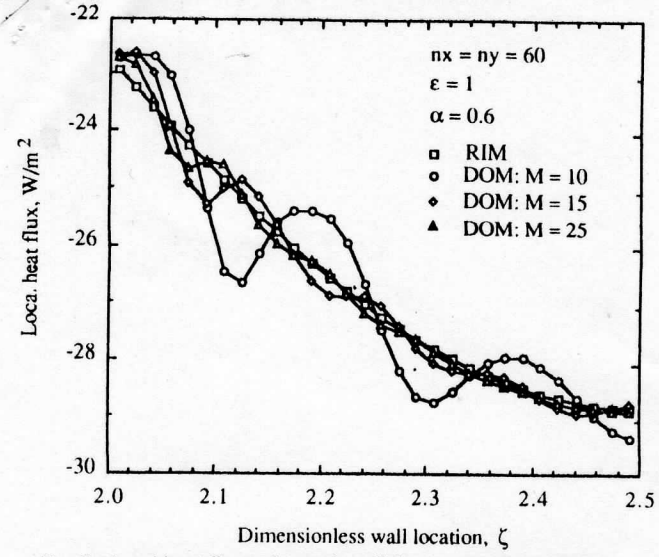

Fig. 4 Local heat fluxes for each wall for rectangular enclosure

the radiative properties of the interface and control volumes are adjusted to accommodate each geometry.

For the DOM, all enclosures are divided into nx and ny control volumes for the x and y directions, respectively. For the RIM, all horizontal and vertical walls of the enclosure are divided into nx and ny surfaces, respectively. The obstruction and protrusion surfaces are divided into elemental areas equal to those of the opposite enclosure walls.

Rectangular Enclosure. For the first test case, a square rectangular enclosure with $H = L = 1.0$ m is examined. The walls of the enclosure are maintained at isothermal temperatures of $T_w = 310$ K and $T_n = T_e = T_s = 300$ K. All surfaces are black. The uniformity assumption of the wall temperature and emittance distributions may be relaxed because DOM and RIM are capable of handling arbitrary distributions. In addition, $\alpha = 0.6$, $M = 15$, and $nx = ny = 60$. The number of surfaces for the indicated grid is $N = 240$. The effects of these parameters are identified later. Unless otherwise noted, these conditions apply to the results. Because the west wall views an isothermal enclosure, heat fluxes are equal to a constant given by the difference of blackbody emissive powers evaluated at temperatures of 310 and 300 K. The other walls experience a negative heat flux that is a function of how well a surface element views the heated wall.

Heat fluxes from the DOM predict exactly those from the RIM for the west wall and are nearly indistinguishable from those of the RIM for the north and east walls. An indication of the agreement of the heat fluxes for the two methods is shown in Fig. 4, using expanded scales, where heat fluxes for the upper half of the east wall ($2.0 \le \zeta \le 2.5$) are shown. The dimensionless wall distance ζ has its origin at the lower-left-hand corner of the west wall in Fig. 1 and extends clockwise around the enclosure. In addition to heat fluxes for $M = 15$, heat fluxes are shown for $M = 10$ and 25. For $M = 10$, significant oscillations of the heat fluxes for the DOM about those of the RIM are found. The maximum error between the RIM and DOM results for this wall section is -6.32 percent found at $\zeta = 2.117$. The oscillations tend to be more noticeable for surface elements near a corner ($\zeta = 2.0$). The oscillations and errors diminish, however, as the number of discrete angles increases. For example, for $M = 25$, the maximum error is -0.84 percent occurring at $\zeta = 2.067$.

Overall heat fluxes for a wall area may be predicted rather accurately by a low number of discrete angles. This is illustrated in Table 2, where heat fluxes for the DOM and RIM are presented for the north (same as south) and east walls. Heat

Table 2 Overall heat fluxes

DOM M	Heat flux, W/m^2 north	east
10	-18.844	-26.667
15	-18.834	-26.687
20	-18.824	-26.708
25	-18.820	-26.716
	(-18.876)*	(-26.603)
50	-18.814	-26.727
	(-18.849)	(-26.656)
RIM	-18.849	-26.657

*Numbers in parentheses are for $\alpha = 0.5$.

fluxes for the DOM are provided for $\alpha = 0.6$ and $M = 10$, 15, 20, 25, and 50. The numbers in parentheses are discussed in the next paragraph. The error for the north and east walls is less than 0.04 percent for $M = 10$ and deteriorates to near 0.2 percent for $M = 25$. The error for larger values of M ($= 50$) never exceeds 0.27 percent. A portion of these errors is attributed to the DOM computing the radiant exchange for a point on a surface element, whereas the view factors are integrated values.

As identified later, the accuracy of the DOM depends on, among other factors, the number of discrete angles and the finite-difference weighting factor. Overall heat fluxes shown in parentheses in Table 2 for $\alpha = 0.5$ when $M = 25$ and 50 illustrate the latter effect. For $\alpha = 0.5$, the errors in the overall heat fluxes are less than 0.21 percent for $M = 25$ and are nearly zero percent for $M = 50$. Hence, through adjustment of the finite-difference weighting factor and the selection of the number of discrete angles, the DOM is capable of predicting accurate heat fluxes.

To identify further the error between local fluxes computed using the RIM and DOM and to examine the influence on the error of the emittance, finite-difference weighting factor, number of discrete angles, and grid, the root-mean-square (rms) error is computed using

$$e_{\text{rms}} = \left[\frac{1}{N-1} \sum_{i=1}^{N} \left(\frac{q_{\text{RIM},i} - q_{\text{DOM},i}}{q_{\text{RIM},i}} \right)^2 \right]^{1/2} \tag{17}$$

where the subscripts RIM and DOM refer to heat fluxes computed using the RIM and DOM. The rms errors are displayed in Fig. 5 as a function of the finite-difference weighting factor for $nx = ny = 20$ and 60 and for $\epsilon = 1.0$, 0.5, and 0.1, where all walls have the same emittance. Heat fluxes for the DOM are for $M = 25$. Consider first the rms errors for $\epsilon = 1.0$. As α increases from 0.5, the rms error decreases, reaches a minimum, and then increases. The minimum rms errors occur near $\alpha = 0.54$ and 0.62 for the coarser and finer grids, respectively, and are nearly identical at a value of 0.32 percent for the two grids. For $M = 50$ and the finer grid (not shown), the minimum rms error is 0.13 percent found at $\alpha = 0.54$, and at $\alpha = 0.6$, it is 0.20 percent.

From Fig. 5, the rms errors diminish as the emittance is decreased. The minimum rms errors for $\epsilon = 0.5$ and 0.1 are 0.18 and 0.035 percent, respectively. The value of α that yields a minimum rms error for a given grid is nearly independent of emittance. As an example, for the finer grid, the minimum rms errors occur near $\alpha = 0.62$ for $\epsilon = 1.0$, 0.5, and 0.1. The effect of the emittance on the local heat fluxes is examined further for Case 2.

The influence of the number of discrete angles on the local heat fluxes is presented in Fig. 6 for $\alpha = 0.6$, $nx = ny = 60$, and $\epsilon = 1.0$. Heat flux results for the DOM and RIM are shown at spatial locations of $\zeta = 1.0167$ (west end of the north wall), 1.4833 (center of north wall), 1.9833 (east end of north wall), 2.0167 (north end of east wall), and 2.4833 (center of east

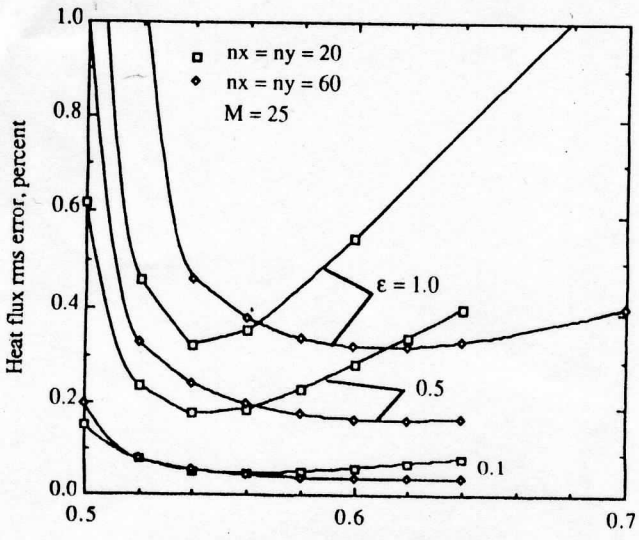

Fig. 5 The rms errors for rectangular enclosure

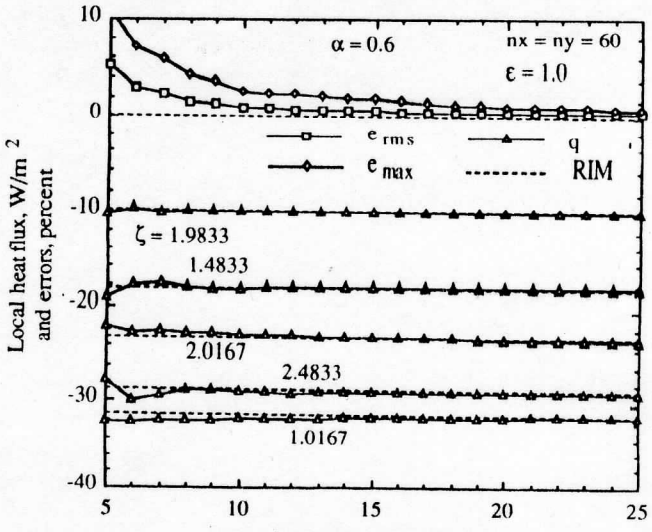

Fig. 6 Influence of number of discrete angles

wall). Also, the rms error and the absolute maximum error (e_{max}) in local heat fluxes for the DOM are illustrated. The oscillatory behavior with decreasing amplitude of oscillation of some of the DOM heat fluxes as M increases is shown in the figure. For $M > 15$, local fluxes for the DOM are in good agreement with the RIM results for the indicated positions. The maximum error shows a decreasing trend as M increases. For $M > 14$, the maximum error is less than 2 percent and the rms error is less than 0.7 percent. For $M = 25$, the maximum error is less than 1.0 percent.

The control volumes used for the results in Figs. 4–6 are square. In some applications, it may not be desirable or possible to use square control volumes, and the effect of nonsquare control volumes needs to be examined. The rms errors for $L = 0.5$ m, $H = 1.0$ m, $ny = 60$, and $nx = 30$ and 60 were computed for various values of α. Control volumes are square for $nx = 30$ and are twice as high as wide for $nx = 60$. The results are similar to those in Fig. 5. The rms error does depend on the size of the control volume but the dependency is not significant. Minimum rms errors of 0.264 and 0.338 appear near $\alpha = 0.6$ and 0.7 for $nx = 30$ and 60, respectively. For $\alpha < 0.68$, rms errors for the square control volumes are smaller than those for the narrower control volumes. Selecting $\alpha = 0.6$ for both grids yields $e_{rms} < 0.4$ percent.

The computations were performed on an Encore Multimax 320 computer system with a rating of 0.2 MFLOPS. The conditions for $nx = ny = 60$, black walls, and $\alpha = 0.6$ require central processor unit times of 166 and 279 s for $M = 15$ and 25, respectively. The corresponding times for $nx = ny = 20$ are 20 and 34 s. The computational times for the RIM for the finer and coarser grid patterns are 12.4 and 1.8 s. The higher times for the DOM should not penalize the attractiveness of this method because the setup times are significantly lower for this method than those for the RIM.

In the analysis, the equal angle quadrature set is noted to yield more accurate results than other sets. To illustrate this, the S8 quadrature set of Fiveland (1988) corresponding to 10 streams per quadrant is used to solve the rectangular enclosure case with black surfaces and $nx = ny = 60$. For this set, the minimum rms error of 13.4 percent is found at $\alpha = 1.0$. For the equal angle set with $M = 10$, the minimum rms error of 1.01 percent occurs near $\alpha = 0.90$. Hence, the equal angle set does yield more accurate heat fluxes. These findings imply that, for absorbing gases, a different discrete ordinate set should be used to evaluate radiant exchange in the transparent windows than that for the absorbing bands.

In summary, the results for the rectangular enclosure reveal that the DOM is capable of predicting accurate local and overall heat fluxes. As a compromise between computational effort and accuracy, the number of discrete angles could be as low as 15. Also, a value of $\alpha = 0.6$ would yield accurate results for the conditions examined.

Centered Obstruction. The second case involves a square enclosure with a square, centered obstruction. The enclosure has $H = L = 1.0$ m, $T_w = 320$ K, and $T_n = T_e = T_s = 300$ K. The obstruction has sides of length 0.5 m and a temperature of 300 K. All surfaces have the same emittance. Local radiant heat fluxes for the DOM and RIM are displayed in Fig. 7 for emittances of 0.5 and 1.0, $nx = ny = 40$, $\alpha = 0.6$, and $M = 15$. The dimensionless distance ζ has the same origin as in Fig. 4 and continues clockwise around the obstruction. Hence, the north surface of the obstruction lies within the range of $4.5 < \zeta < 5.0$. Because of blockage by the obstruction, the heat flux for $\epsilon = 1.0$ is zero for the east portion of the enclosure wall between $2.375 < \zeta < 2.625$ and for the east surface of the obstruction. Because of symmetry, heat fluxes for only the upper half of the enclosure and obstruction are plotted. There is good agreement between the DOM and RIM results.

Further evidence of the accuracy of the DOM was obtained by examining the heat flux rms error as a function of the finite-difference weighting factor. For these results, all surfaces have the same emittances of 1.0 and 0.5, and $M = 25$. As shown in Fig. 7, heat fluxes for some of the surface elements are zero. Thus, when computing the rms error, surface elements with a zero heat flux for the RIM are excluded from the summation in Eq. (17), and the value of N is reduced accordingly. Also, for the east surface of the enclosure wall, the heat flux is very small for the surface element just prior to the point where the obstruction blocks the view of the heated west wall. Specifically, at $\zeta = 2.3375$, heat fluxes for the RIM and DOM are $q_{RIM} = -0.244$ W/m^2 and $q_{DOM} = 1.548$ W/m^2, which convert to an error of 534 percent. Because the heat fluxes are small, this point and the corresponding point by symmetry are neglected in the summation of Eq. (17). The effect of α on e_{rms} is similar to that shown in Fig. 5. The optimum value of α occurs near 0.55 with rms errors of 1.28 and 0.92 percent for $\epsilon = 1.0$ and 0.5, respectively. These rms errors are larger than those for the rectangular enclosure without the obstruction because the surface elements with zero heat fluxes (for both the DOM and RIM, where there is exact agreement) are excluded from the summation.

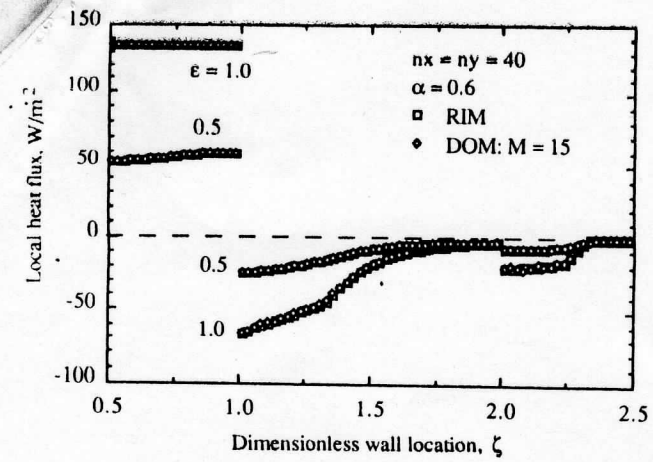

(a) Enclosure walls.

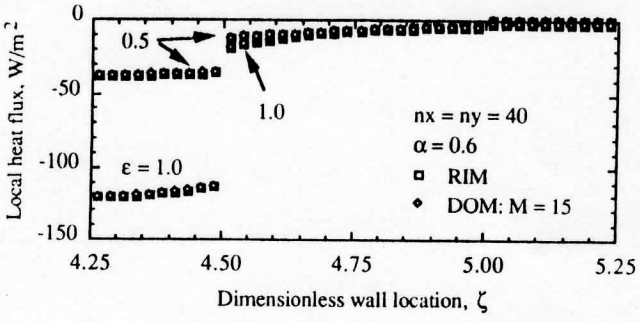

(b) Obstruction surfaces.

Fig. 7 Local heat fluxes for enclosure with obstruction

The influence of the number of discrete angles on the local heat fluxes, rms error, and absolute maximum error was also examined for black surfaces and $\alpha = 0.6$. The effect of M is similar to that in Fig. 6. For $M = 10$ and 25, $e_{rms} = 4.3$ and 1.7 percent, respectively.

Two Protrusions. The third test case was chosen as representative of an electronic chassis containing electronic components (protrusions) mounted on a printed circuit board (Smith et al., 1991). For this case, the rectangular enclosure in Fig. 1 has $H = 50$ mm and $L = 12$ mm. Two protrusions are centered on the west wall in Fig. 1. The protrusions have dimensions of 6 and 15 mm in the x and y directions, respectively, and are separated a distance of 10 mm. Hence, the west wall has exposed areas of 5 mm at the top and bottom and 10 mm at the center. The enclosure walls are assigned temperatures of $T_w = 310$ K and $T_n = T_e = T_s = 300$ K and emittances of $\epsilon_w = 0.9$ and $\epsilon_n = \epsilon_e = \epsilon_s = 0.5$. The protrusions have uniform temperatures of 320 K and emittances of 0.8. The higher temperature of the protrusions could be caused by internal heat generation within the protrusions. Numerical solutions for local radiant fluxes were obtained using $nx = 12$ and $ny = 50$. Local heat fluxes for the DOM and RIM are displayed in Fig. 8 for surface elements in the upper half of the system. Heat fluxes for the DOM are for $M = 15$ and $\alpha = 0.6$. The surface location number K represents the upper half of the west wall between the protrusions for $1 \le K \le 5$, the upper protrusion for $6 \le K \le 32$, the upper portion of the west wall for $33 \le K \le 37$, the north wall for $38 \le K \le 49$, and the upper half of the east wall for $50 \le K \le 74$. There is good agreement between the heat fluxes based on the DOM and RIM.

The influence of the finite difference weighting factor on the heat flux rms error was examined. When computing the rms error, a large error was found at $K = 35$, where $q_{RIM} = 0.00921$ W/m^2 and $q_{DOM} = 0.294$ W/m^2, which converts

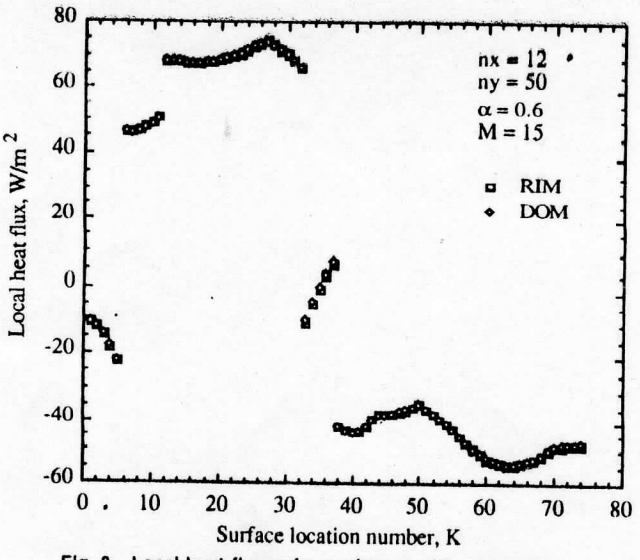

Fig. 8 Local heat fluxes for enclosure with protrusions

to an error of 3090 percent. From Fig. 8, the heat flux at this location is passing through zero. Hence, this location and the resultant error are not included in the summation of Eq. (17). The rms error has the same behavior as in Fig. 5, attaining a minimum of 0.741 percent near $\alpha = 0.55$. For $\alpha = 0.6$, the rms error is 1.56 percent.

The effect of the number of discrete angles on the rms and maximum errors was examined for $\alpha = 0.6$. The rms error is nearly independent of M with values of 1.558 and 1.556 percent for $M = 15$ and 25. For $M > 20$, the maximum error is less than 10 percent and is located at $K = 34$, which is near the point where the heat flux passes through zero.

Conclusions

The discrete-ordinates method has been developed for evaluation of radiant exchange between surfaces separated by a transparent medium. The method uses the control volume approach to track the radiant intensity in discrete directions. The formulation is attractive in that arbitrary arrangements of solid objects separated by a transparent medium can be accommodated by appropriate selection of the radiative properties of the control volumes and of the interfaces between control volumes. Validation of the method was accomplished by comparing local heat fluxes to those computed from the radiosity/irradiation analysis. Three geometric configurations that include effects of shadowing and irregular boundaries are examined. In all comparisons, heat fluxes based on the discrete-ordinates method are in good agreement with those from the analysis. Effects of reflecting surfaces as well as nonsquare control volumes are presented. The comparisons also established that selecting a finite-difference weighting factor of 0.6 and the number of discrete angles of 15 yield accurate results. In the interest of improving and expanding the method, specification of the discrete angles could be re-examined, the method could be extended to surfaces with a bidirectional reflectance, three-dimensional geometries could be examined, and application of the method to radiant exchange when a participating medium separates the surfaces would be of interest.

Acknowledgments

The first author would like to acknowledge the financial support received from Universidad de los Andes and Fundaciòn Gran Mariscal de Ayacucho, both of the Republic of Venezuela. The second author wishes to acknowledge support for this study by Rockwell International Corporation.

References

Baumeister, J. F., 1990, "Thermal Radiation Characteristics of Nonisothermal Cylindrical Enclosures Using a Numerical Ray Tracing Technique," *Radiation Heat Transfer: Fundamentals and Applications*, T. F. Smith, M. F. Modest, A. M. Smith, and S. T. Thynell, eds., ASME HTD-Vol. 137, pp. 73–79.

Billings, R. L., Barnes, J. W., Howell, J. R., and Slotboom, O. E., 1990, "Markov Analysis of Radiative Transfer in Specular Enclosures," *Radiation Heat Transfer: Fundamentals and Applications*, T. F. Smith, M. F. Modest, A. M. Smith, and S. T. Thynell, eds., ASME HTD-Vol. 137, pp. 89–94.

Emery, A. F., Johansson, O., Lobo, M., and Abrous, A., 1991, "A Comparative Study of Methods for Computing the Diffuse Radiation Viewfactors for Complex Structures," ASME JOURNAL OF HEAT TRANSFER, Vol. 101, pp. 413–422.

Fiveland, W. A., 1988, "Three-Dimensional Radiative Heat-Transfer Solutions by the Discrete-Ordinates Method," *Journal of Thermophysics and Heat Transfer*, Vol. 2, pp. 309–316.

Greenberg, D. P., 1989, "Light Reflection Models for Computer Graphics," *Science*, Vol. 244, pp. 166–173.

House, J. M., Beckermann, C., and Smith, T. F., 1990, "Effect of a Centered Conducting Body on Natural Convection Heat Transfer in an Enclosure," *Numerical Heat Transfer*, Part A, Vol. 18, pp. 213–225.

Modest, M. F., 1991, "The Weighted-Sum-of-Gray-Gases Model for Arbitrary Solution Methods in Radiative Transfer," *ASME/JSME Thermal Engineering Proceedings*, Vol. 4, pp. 3–10.

Naraghi, M. H. N., and Chung, B. T. F., 1984, "A Stochastic Approach for Radiative Exchange in Enclosures With Nonparticipating Medium," ASME JOURNAL OF HEAT TRANSFER, Vol. 106, pp. 690–698.

Naraghi, M. H. N., and Chung, B. T. F., 1986, "A Stochastic Approach for Radiative Exchange in Enclosures With Directional-Bidirectional Properties," ASME JOURNAL OF HEAT TRANSFER, Vol. 108, pp. 264–270.

Patankar, S. V., 1990, *Numerical Heat Transfer and Fluid Flow*, McGraw-Hill, New York.

Rushmeier, H. E., Baum, D. R., and Hall, D. E., 1990, "Accelerating the Hemi-Cube Algorithm for Calculating Radiation Form Factors," *Radiation Heat Transfer: Fundamentals and Applications*, T. F. Smith, M. F. Modest, A. M. Smith, and S. T. Thynell, eds., ASME HTD-Vol. 137, pp. 45–51.

Sànchez, A., Smith, T. F., and Krajewski, W. F., 1991, "Three-Dimensional Radiative Heat Transfer in a Polydispersion With Collimated Incident Source," accepted for the 1991 National Heat Transfer Conference.

Siegel, R., and Howell, J. R., 1981, *Thermal Radiation Heat Transfer*, Hemisphere Publishing, Washington, DC.

Smith, T. F., Beckermann, C., and Weber, S. W., 1991, "Combined Conduction, Natural Convection, and Radiation Heat Transfer in an Electronic Chassis," ASME *Journal of Electronic Packaging*, Vol. 113, pp. 382–391.

Sparrow, E. M., and Cess, R. D., 1978, *Radiation Heat Transfer*, Hemisphere Publishing, New York.

Truelove, J. S., 1987, "Discrete-Ordinate Solutions of the Radiation Transport Equation," ASME JOURNAL OF HEAT TRANSFER, Vol. 109, pp. 1048–1051.

Walton, G. N., 1987, "Algorithms for Calculating Radiation View Factors Between Plane Convex Polygons With Obstructions," *Fundamentals and Applications of Radiation Heat Transfer*, A. M. Smith and T. F. Smith, eds., ASME HTD-Vol. 72, pp. 45–52.